Two-Path Interference for Enantiomer-Selective State Transfer of Chiral Molecules

Jin-Lei Wu,[1] Yan Wang,[1] Jin-Xuan Han,[1] Cong Wang,[1] Shi-Lei Su,[2] Yan Xia,[3] Yongyuan Jiang,[1,*] and Jie Song[1,4,5,†]

[1] *School of Physics, Harbin Institute of Technology, Harbin 150001, China*
[2] *School of Physics, Zhengzhou University, Zhengzhou 450001, China*
[3] *Department of Physics, Fuzhou University, Fuzhou 350002, China*
[4] *Key Laboratory of Micro-Nano Optoelectronic Information System, Ministry of Industry and Information Technology, Harbin 150001, China*
[5] *Key Laboratory of Micro-Optics and Photonic Technology of Heilongjiang Province, Harbin Institute of Technology, Harbin 150001, China*

(Received 21 October 2019; revised manuscript received 5 March 2020; accepted 23 March 2020; published 8 April 2020)

Using a microwave-regime cyclic three-state configuration, enantiomer-selective state transfer (ESST) is carried out through two-path interference between a direct one-photon coupling and an effective two-photon coupling. A phase difference of π in the one-photon process between the two enantiomers makes the interference constructive for one enantiomer but destructive for the other. Therefore only one enantiomer is excited into a higher rotational state, while the other remains in the ground state. The scheme allows flexibility in the pulse waveforms and the time order of the two paths. We simulate the scheme for a sample of cyclohexylmethanol ($C_7H_{14}O$) molecules. The simulation results show that robust high-fidelity ESST can be obtained when experimental concerns are considered. Finally, we propose to employ the ESST scheme to implement enantioseparation and determine enantiomeric excesses.

DOI: 10.1103/PhysRevApplied.13.044021

I. INTRODUCTION

Although two enantiomers, namely a chiral molecule and its mirror image, may share many physical and chemical properties, living creatures treat them as different molecules because of their divergent biological activities and functions. This biological enantioselective characteristic of chiral molecules has been recognized as important for chemistry [1–3], biotechnology [4–6], and pharmaceutics [7–10]. So, the property of chirality is one of the most profound aspects of the world, and enantiomer-selective tasks on chiral molecules, e.g., enantiomer separation, enantiomer purification, absolute-configuration determination, and enantiomeric excess determination, are of great significance. In addition to the widely used purely chemical means [11–16], optical methods are potential candidates for performing enantiomer-selective tasks on chiral molecules [17–22]. Some spectroscopic techniques have been established for the determination of the absolute configuration and enantiomeric excess of a chiral sample, such as techniques based on circular dichroism [23], vibrational circular dichroism [24], and Raman optical activity [25]. However, these techniques depend on interference between electric dipole and weak magnetic dipole transitions, or in some cases between electric dipole and weak electric quadrupole transitions. Therefore these techniques generally require high-density samples [26–28]. To obtain enhanced probe signals, chiral molecules have also been widely studied using other spectroscopic techniques, e.g., ultrafast resonant x-ray spectroscopy [29,30] and the study of Raman optical activity by coherent anti-Stokes Raman-scattering spectral interferometry [31,32].

Recently, alternative schemes based on a cyclic three-state configuration with three rotational transitions in the microwave regime have been considered promising. A method for coherently controlled adiabatic passage [33–35], termed "cyclic population transfer" (CPT), is of importance and interest. However, although this method may enable highly efficient enantiomer-selective tasks by following the concepts of adiabatic passage techniques [36,37], it is usually slow and complicated. Fast schemes with nonadiabatic dynamics using resonant ultrashort pulses have been proposed [38–40]. Lately, many remarkable experiments have contributed to the verification of enantiomeric differentiation and probing of enantiomeric excesses based on the technique of microwave three-wave mixing (M3WM) [41–48]. Promoted by experimental

*jiangyy@hit.edu.cn
†jsong@hit.edu.cn

achievements, some proposals have been put forward very recently for related issues, such as the design of cyclic three-level configurations for chiral molecules [49], shortcut-to-adiabatic (STA) enantiomer-selective population transfer of chiral molecules by means of shaped pulses [50,51], and dynamic methods for enantiomeric excess determination [40] and the inner-state enantioseparation [52].

Enantiomer-selective state transfer (ESST) is the premise of many schemes for enantiomer separation [50], enantiomer purification [33,34], and enantiomeric excess determination [46,47]. In this paper, a two-path interference approach is proposed for ESST of chiral molecules using a cyclic three-state configuration $|1\rangle \leftrightarrow |2\rangle \leftrightarrow |3\rangle \leftrightarrow |1\rangle$ with three rotational levels. Two enantiomers are both prepared initially in the ground state $|1\rangle$, but finally evolve along two interfering paths into entirely different states. The two interfering paths are formed by a direct one-photon $|1\rangle \leftrightarrow |3\rangle$ coupling and an effective two-photon coupling with the intermediate state $|2\rangle$. A phase difference of π between the two enantiomers in the one-photon coupling makes the two-path interference constructive for one enantiomer but destructive for the other. Therefore only one of the two enantiomers is excited into the excited state $|3\rangle$, while the other remains in the ground state $|1\rangle$.

The present scheme is performed in the nonadiabatic regime and thus is faster than slow adiabatic schemes [33,34]. Unlike the case of nonadiabatic dynamic methods [38,39,46–48,52], the one- and two-photon processes can be performed synchronously or consecutively, without relying on a fixed time order. Besides, by means of pulse engineering, we use shaped pulses in the scheme to enhance its efficiency and robustness. In addition, compared with STA schemes [50,51], the present approach allows flexibility in the waveforms as well in as the time order of the two coupling paths. As an example, we apply this two-path interference scheme to a sample of cyclohexylmethanol ($C_7H_{14}O$) molecules, and experimental issues concerning unwanted transitions, imperfect initial states, pulse shaping, control errors, and the finite lifetimes of higher energy levels are discussed. Simulation results indicate that robust and highly efficient ESST of cyclohexylmethanol molecules can be obtained. Further possible tasks of enantiomer separation and M3WM-assisted determination of enantiomeric excesses after the ESST is finished are discussed.

II. TWO-PATH-INTERFERENCE APPROACH

A. Two enantiomers interacting with three orthogonal microwave fields

A cyclic three-state configuration for two enantiomers is shown in Fig. 1, in which three rotational energy states $|1\rangle$, $|2\rangle$, and $|3\rangle$ are considered for each enantiomer. The

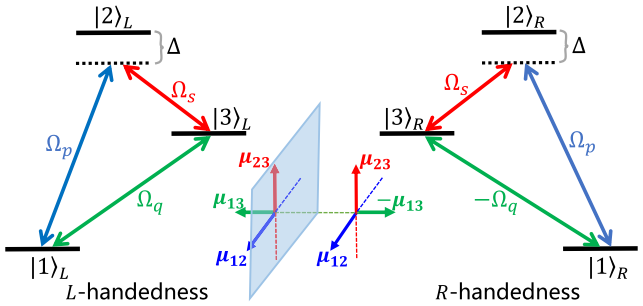

FIG. 1. Couplings among three rotational energy states for the two enantiomers of a chiral molecule. Three orthogonal microwave fields are imposed, which drive three corresponding types of transition with orthogonal electric dipole moments. The electric dipole moments of the two enantiomers are mirror images of each other.

electric-dipole-allowed transitions $|1\rangle \leftrightarrow |2\rangle$, $|1\rangle \leftrightarrow |3\rangle$, and $|2\rangle \leftrightarrow |3\rangle$ have individual dipole moments $\vec{\mu}_{12}$, $\vec{\mu}_{13}$, and $\vec{\mu}_{23}$. Because the moments of inertia of molecules determine their rotational spectra, molecular rotational spectra depend on the distribution of atomic masses in the molecules. Therefore, rotational spectroscopy is sensitive to even tiny changes in the structure or masses. Correspondingly, the three types of electric dipole moment of one enantiomer are mirror images of their counterparts for the other enantiomer due to their asymmetric distributions of atoms [53].

Three orthogonal microwave fields p, q, and s irradiate molecules of the two enantiomers to drive the three rotational transitions, with individual Rabi frequencies Ω_p, Ω_q, and Ω_s, as shown in Fig. 1. The strength of field j $(j = p, q, s)$ is expressed by $\vec{E}_j = \vec{e}_j \varepsilon_j \cos(\omega_j t + \phi_j)$, where $\vec{e}_j$, ε_j, ω_j, and ϕ_j are the unit vector, amplitude, frequency, and phase, respectively. Correspondingly, $\Omega_p \equiv \vec{\mu}_{12} \cdot \vec{e}_p \varepsilon_p$, $\Omega_q \equiv \vec{\mu}_{13} \cdot \vec{e}_p \varepsilon_p$, and $\Omega_s \equiv \vec{\mu}_{23} \cdot \vec{e}_p \varepsilon_p$.

Here, we choose $|1\rangle$ as the zero-energy point and use natural units with $\hbar = 1$ for simplicity. The Hamiltonian of the cyclic three-state configuration can be represented as

$$\hat{H}_0 = \omega_{12}|2\rangle\langle 2| + \omega_{13}|3\rangle\langle 3| + \Big(\vec{\mu}_{12} \cdot \vec{E}_p |1\rangle\langle 2| + \vec{\mu}_{13} \cdot \vec{E}_q |1\rangle\langle 3| + \vec{\mu}_{23} \cdot \vec{E}_s |2\rangle\langle 3| + \text{H.c.}\Big), \quad (1)$$

where $\omega_{1,n}$ $(n = 2, 3)$ is the $|1\rangle \leftrightarrow |n\rangle$ transition frequency. Owing to the mirror-reflection relationship of the electric dipole moments of the two enantiomers, the triple product $\vec{\mu}_{12} \cdot (\vec{\mu}_{13} \times \vec{\mu}_{23})$ is of opposite sign for the two enantiomers. For convenience, we specify the model such that $\vec{\mu}_{12}$ and $\vec{\mu}_{23}$ have identical orientations for the two enantiomers, while $\vec{\mu}_{13}$ has opposite orientations, as shown in Fig. 1, which results in the two enantiomers having identical Ω_p and Ω_s but opposite-sign Ω_q. In the

laboratory frame, this can be achieved by choosing a suitable set of axes, as in a recent experiment [46]. Alternatively, one can choose a suitable group of phases of the three microwave fields, as in another recent experiment [48]. Hereinafter, we consider the following conditions: (i) rotating-wave approximation, $\omega_j \gg |\Omega_j|$; (ii) resonant $|1\rangle \leftrightarrow |3\rangle$ one-photon transition, $\omega_{13} = \omega_q$; and (iii) resonant $|1\rangle \leftrightarrow |3\rangle$ two-photon transition but off-resonant $|1\rangle \leftrightarrow |2\rangle$ and $|2\rangle \leftrightarrow |3\rangle$ one-photon transitions, $\omega_{12} - \omega_p = \omega_{23} - \omega_s = \Delta$.

B. Enantiomer-selective state transfer through two-path interference

In the rotating-wave approximation, the Hamiltonian [Eq. (1)] can be written in the interaction picture for the two enantiomers as

$$\hat{H}_{L,R} = \left(\frac{\Omega_p}{2}|2\rangle\langle 1| + \frac{\Omega_s}{2}|2\rangle\langle 3|\right)e^{i\Delta t} \pm \frac{\Omega_q}{2}|1\rangle\langle 3| + \text{H.c.}, \tag{2}$$

where the subscripts L and R denote left- and right-handedness, respectively. We choose the phases of all three microwave pulses as zero. The last term describes a direct $|1\rangle \leftrightarrow |3\rangle$ coupling by a one-photon process, and the two enantiomers differ in their Rabi frequency Ω_q by a phase π. The identical first term denotes the detuned $|1\rangle \leftrightarrow |2\rangle$ and $|2\rangle \leftrightarrow |3\rangle$ transitions, with detuning Δ, but the two-photon $|1\rangle \leftrightarrow |3\rangle$ transition is resonant.

We aim to form an effective two-photon $|1\rangle \leftrightarrow |3\rangle$ coupling that can interfere with the direct one-photon coupling. Therefore, interference between the one-photon transitions $|1\rangle \leftrightarrow |3\rangle$ and $|1\rangle \leftrightarrow |2\rangle$ or $|2\rangle \leftrightarrow |3\rangle$ has to be absent, because it causes the one-photon transition $|1\rangle \leftrightarrow |3\rangle$ to be not only governed by the pulse q but also affected by the pulses p and s. A valid way is to eliminate the occupation of the intermediate state $|2\rangle$ during the two-photon process $|1\rangle \leftrightarrow |2\rangle \leftrightarrow |3\rangle$, which can make the one- and two-photon processes independent of each other. Then, under the large-detuning condition $\Delta \gg \Omega_p, \Omega_s$, the dynamics of the two enantiomers is dominated by the following effective Hamiltonian (see Appendix A for details):

$$\hat{H}^e_{L,R} = \frac{\Omega_q \mp \Omega_{\text{eff}}}{2}|1\rangle\langle 3| + \text{H.c.}, \tag{3}$$

with $\Omega_{\text{eff}} \equiv \Omega_p\Omega_s/2\Delta$. Since the two enantiomers differ in their one-photon coupling by a phase difference of π, the two paths interfere with each other constructively for right-handed molecules but destructively for left-handed molecules. We assume that the operation starts at $t = 0$ and ends at $t = T$. If we control the pulse areas of the three microwave pulses so as to satisfy

$$\int_0^T \frac{\Omega_q - \Omega_{\text{eff}}}{2}dt = n_l\pi, \quad \int_0^T \frac{\Omega_q + \Omega_{\text{eff}}}{2}dt = \left(n_r + \frac{1}{2}\right)\pi, \tag{4}$$

with n_l and n_r being integer numbers, right-handed molecules will be excited into $|3\rangle$ while left-handed molecules remain in or evolve back to $|1\rangle$, which means the implementation of ESST. This ESST is achieved by the interference of transitions rather than by the CPT commonly used in existing schemes [33,34,38,39,47,48,50–52].

III. PULSE ENGINEERING

A. Efficiency of state transfer with shaped pulses

High efficiency is one of the advantages of enantiomer-selective schemes based on microwave-regime rotational spectroscopy, because the pure electric dipole couplings allow strong molecule-field interactions and intense chiral molecular signals. In order to ensure faithful two-path interference, the ratio Δ/Ω_0 should in theory be as large as possible, with $\Omega_0 \equiv \max\{\Omega_p, \Omega_s\}$ being the maximum amplitude of the Rabi frequencies Ω_p and Ω_s. In practice, however, it is unnecessary to adopt a very large ratio Δ/Ω_0, and a relatively high efficiency can nevertheless be obtained.

In order to get a moderate ratio Δ/Ω_0, we now consider solely the use of the two-photon coupling to excite all molecules from $|1\rangle$ into $|3\rangle$, and assume that the partial Hamiltonian $\hat{h}(t) = (\Omega_p|2\rangle\langle 1| + \Omega_s|2\rangle\langle 3|)e^{i\Delta t}/2 +$ H.c. governs the evolution. For square pulses p and s with $\Omega_p = \Omega_s = \Omega_0$, the pulse area should satisfy $\int_0^T \Omega_{\text{eff}}\,dt = \pi$, i.e., $T = 2\pi\Delta/\Omega_0^2$, to ensure that all molecules are excited into $|3\rangle$. In Fig. 2 (solid red line), we plot the

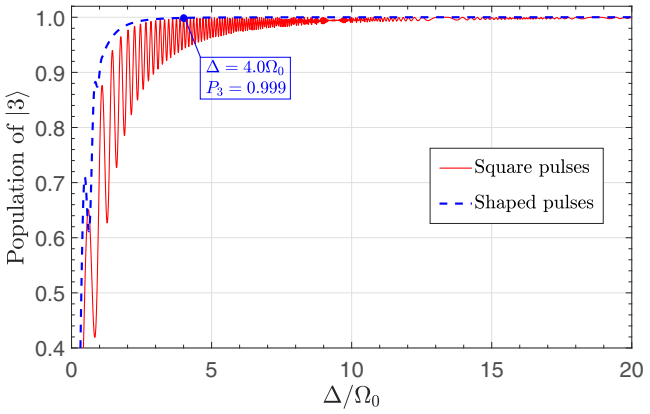

FIG. 2. Final population of $|3\rangle$ for all molecules excited through only the two-photon process for varying Δ/Ω_0, for square (solid red line) or shaped (blue dashed line) pulses p and s.

final ($t = T$) population of $|3\rangle$ for all molecules for varying Δ/Ω_0. When the ratio Δ/Ω_0 reaches a certain value (about 10), the final population of $|3\rangle$ becomes near unity. For $\Delta = 10\Omega_0$, the effective strength of the two-photon $|1\rangle \leftrightarrow |3\rangle$ coupling is $\Omega_{\rm eff} = 0.05\Omega_0$, which is smaller than the original strength by nearly two orders of magnitude.

Recently, pulse engineering has been widely studied in a search for robust dynamics and steady quantum states [54–56]. Here, we use pulse engineering to enhance the efficiency of ESST by replacing square pulses with shaped pulses that are turned on and off smoothly. The waveforms of pulses p and s can be chosen as a single-period cosinelike function

$$\Omega_p = \Omega_s = \begin{cases} \dfrac{\Omega_0}{2}\left(1 - \cos\dfrac{2\pi t}{T_0}\right), & 0 \leqslant t \leqslant T_0, \\ 0, & \text{otherwise}, \end{cases} \tag{5}$$

with T_0 being the period. Then, with $T = T_0 = 16\pi\Delta/3\Omega_0^2$, the final population of $|3\rangle$ for varying Δ/Ω_0 is calculated and is plotted in Fig. 2 (dashed blue line). It is apparent that the final population of $|3\rangle$ can reach a value very near unity as long as $\Delta/\Omega_0 > 2$. There are few oscillations once the final population of $|3\rangle$ becomes near unity, which denotes robust state transfer. Furthermore, when $\Delta/\Omega_0 > 4$, the final population of $|3\rangle$ can be over 0.999. For $\Delta = 4\Omega_0$, the two-photon coupling strength is $\Omega_{\rm eff} = 0.125\Omega_0$, which is smaller than the original strength by just one order of magnitude.

The strengths of magnetic dipole and electric quadrupole transitions are five and six orders of magnitude weaker, respectively, than that of electric dipole transitions. Therefore, the efficiency of the present scheme based on square pulses is about three or four orders of magnitude higher than that of the conventional scheme based on circular dichroism, and comparable to that for photoelectron circular dichroism [57]. The scheme using pulse engineering can work better than a scheme based on photoelectron circular dichroism, and the efficiency is over four orders of magnitude higher than that of the conventional scheme based on circular dichroism.

B. Flexibility in the pulse waveforms and the time order of the two paths

With the two interfering paths established, the conditions for achieving ESST are listed in Eq. (4). The conditions are not limited by the waveforms of the three pulses or even the time order of the two paths, which is different from the situation for the existing adiabatic [33,34], nonadiabatic [38,46–48,52], and STA schemes [50,51]. To test this, we choose different waveforms for pulse q combined with the waveforms in Eq. (5) for pulses p and s to exhibit the flexibility in the pulse waveforms and the time order of the two paths. Typically, we choose $n_l = n_r = 0$ hereinafter so as to achieve the state transfer in a short duration, and this requires $\int_0^T \Omega_q\, dt = \int_0^T \Omega_{\rm eff}\, dt = \pi/2$, which gives $T_0 = 8\pi\Delta/3\Omega_0^2$. We consider several examples of the waveform of pulse q:

(i) a single-period cosinelike waveform imposed after the two-photon effective coupling is finished:

$$\Omega_q = \begin{cases} \dfrac{\Omega_0'}{2}\left[1 - \cos\dfrac{2\pi(t - T_0)}{T_0'}\right], & T_0 \leqslant t \leqslant T_0 + T_0', \\ 0, & \text{otherwise}, \end{cases} \tag{6}$$

with Ω_0' being the maximum amplitude, T_0 (the period of Ω_p and Ω_s) the delay, and $T_0' = \pi/\Omega_0'$ the period, making $T = T_0 + T_0'$;

(ii) a Gaussian waveform with a delay relative to $\Omega_{\rm eff}$:

$$\Omega_q = \Omega_0' \exp\left[-(t - 3t_c)^2/t_c^2\right], \tag{7}$$

with $t_c = \sqrt{\pi}/2\Omega_0'$ being the width, and $T = \max\{6t_c, T_0\}$;

(iii) a single-period $\cos^2$-like waveform completely coinciding with $\Omega_{\rm eff}$:

$$\Omega_q = \begin{cases} \dfrac{\Omega_0'}{4}\left(1 - \cos\dfrac{2\pi t}{T_0}\right)^2, & 0 \leqslant t \leqslant T_0, \\ 0, & \text{otherwise}, \end{cases} \tag{8}$$

with $\Omega_0' = \Omega_0^2/2\Delta$ being the maximum amplitude, and $T = T_0$.

The three example waveforms in Eqs. (6)–(8) of pulse q, combined with $\Omega_{\rm eff}$ and the waveform in Eq. (5) of pulses p and s, are shown in Figs. 3(a), 3(c), and 3(e).

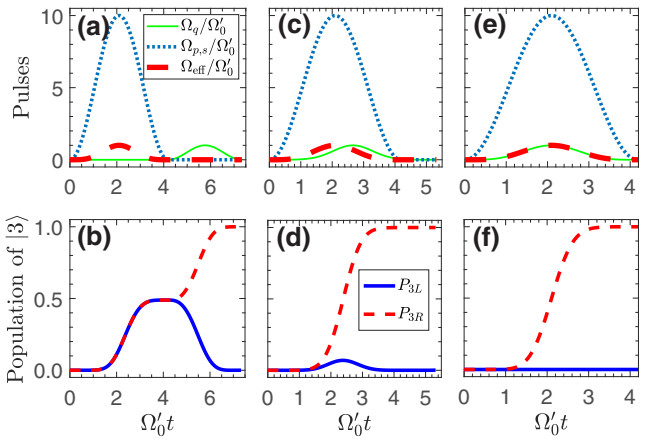

FIG. 3. (a),(c),(e) Shapes of Ω_p, Ω_s, Ω_q, and $\Omega_{\rm eff}$. For Ω_q, the shapes in (a),(c),(e) are those of the waveforms in Eqs. (6), (7), and (8), respectively. (b),(d),(f) Time evolution of the population of $|3\rangle$ for left-handed (solid blue line) and right-handed (dashed red line) molecules. Parameters: $\Omega_0 = 10\Omega_0'$ and $\Delta = 50\Omega_0'$.

For these waveforms, we plot the time evolution of the population of $|3\rangle$ for the two enantiomers (P_{3L} for left-handedness and P_{3R} for right-handedness) in Figs. 3(b), 3(d), and 3(f), correspondingly. We learn that all three sets of pulse waveforms can be used to guarantee that right-handed molecules are excited into $|3\rangle$ from $|1\rangle$ but left-handed ones are unchanged. This illustrates that the present two-path interference scheme for ESST possesses flexibility in the pulse waveforms and the time order of the two paths.

IV. SIMULATION WITH CYCLOHEXYLMETHANOL MOLECULES

In this section, we simulate the two-path interference scheme by using a cyclic three-state configuration $|1_{01}\rangle \leftrightarrow |2_{12}\rangle \leftrightarrow |2_{02}\rangle \leftrightarrow |1_{01}\rangle$ with cyclohexylmethanol ($C_7H_{14}O$) molecules, which has been used in a supersonic jet experiment for CPT in the 2–8-GHz microwave regime [48]. A diagram of the mirror-reflection molecular structures of the two enantiomers is shown in Fig. 4(a), and the cyclic three-state configuration is shown in Fig. 4(b). The energy levels are designated by $|J_{K_a,K_c}\rangle$, where J is the rotational quantum number and K_a and K_c are the projections of J onto the principal axes of the molecule. The two enantiomers have conformer constants $A = 3898.45$ MHz, $B = 1319.59$ MHz, and $C = 1062.55$ MHz. There are three types of rotational transition, a-type, b-type, and c-type, with dipole moments $|\mu_a| = 0.4$ D, $|\mu_b| = 1.2$ D, and $|\mu_c| = 0.8$ D, respectively. We define $|1\rangle \equiv |1_{01}\rangle$, $|2\rangle \equiv |2_{12}\rangle$, and $|3\rangle \equiv |2_{02}\rangle$ to make Figs. 1 and 4(a) coincident. Another state, $|4\rangle \equiv |1_{11}\rangle$, is also considered, because it is involved in two possible unwanted transitions. In the following, by means of the master equation (see Appendix B for details), we simulate the effect of some possible factors on the performance of the two-path interference scheme for ESST.

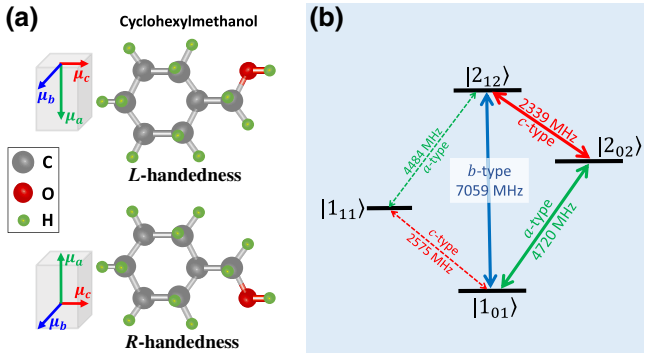

FIG. 4. (a) Diagram of the mirror-reflection molecular structures of the two enantiomers of the cyclohexylmethanol molecule. The orientations of the electric dipole moment of three types of rotational transition are depicted in the adjacent insets. (b) Cyclic three-state configuration (solid thick arrows) for the cyclohexylmethanol molecules, and unwanted transitions (dashed thin arrows).

A. Pulse shaping with a finite time resolution

With an arbitrary-waveform generator, the shapes of the three pulses can be obtained by modulating the field amplitudes by applying voltages to electro-optic modulators [58,59]. Referring to the three transition dipole moments, we choose $\Omega_0 = 12$ MHz and $\Omega_0' = 2$ MHz to simulate the ESST of cyclohexylmethanol molecules. The waveforms of the three pulses given in Eqs. (5) and (7) are chosen, with $T = T_0 = 3.5$ μs and $t_c = 0.443$ μs.

Continuously varying waveforms are desired but are usually unrealistic. In Fig. 5(a), we plot the waveforms of three pulses obtained by introducing a finite time resolution $dt = 50$ ns, and thus each waveform consists of a series of square pulses with a 50-ns duration. Then, we substitute the waveforms in Fig. 5(a) into the master equation and assume the energy relaxations to be absent. The time evolution of the ESST of a cyclohexylmethanol sample is exhibited in Fig. 5(b), where the performance (or fidelity) of the ESST is measured by the quantity

$$\mathcal{D} = |P_{3L} - P_{3R}|\,. \tag{9}$$

The fidelity of the ESST increases with time, and a high-fidelity ESST with $\mathcal{D} = 0.993$ is finally shown. As a matter of fact, the time resolution $dt = 50$ ns used here is far larger than that reported in recent experiments. Arbitrary-waveform generators can achieve a minimum time resolution of approximately 0.25 ns [58] or even 0.1 ns [59]. Therefore, in the following, we can safely assume a time resolution $dt = 10$ ns for the waveforms of the three pulses.

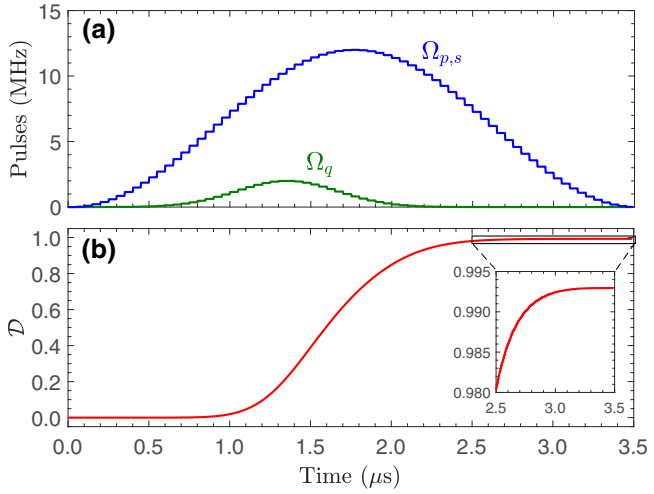

FIG. 5. (a) Waveforms of three pulses with a time resolution $dt = 50$ ns. (b) Time evolution of $\mathcal{D}$ using the pulse waveforms in (a). Parameters without energy relaxations: $\Omega_0 = 12$ MHz, $\Omega_0' = 2$ MHz, $T_0 = 3.5$ μs, $t_c = 0.443$ μs, and $\Delta = 60$ MHz.

B. Errors in amplitudes and frequencies of pulses

In experiments, it is inevitable that the operations on the three pulses will suffer from errors originating from imprecise apparatus, imperfect control, and various unpredictable fluctuations, and so it is essential to investigate the effect of errors in the three pulses on the ESST performance. Here, we are mainly concerned with random amplitude noise and frequency drift.

Because of uncontrollable factors such as mixing of stray light and instability in the voltages, the three pulses may be disturbed by additive white Gaussian noise (AWGN) and random fluctuations. The AWGN-mixed Rabi frequency is written as

$$\Omega_{\mathrm{AWGN}}(t) = \Omega(t) + \mathrm{awgn}[\Omega(t),\ R_{\mathrm{SN}}], \tag{10}$$

where awgn is the generation function of the AWGN mixed into the original pulse $\Omega(t)$, with a signal-to-noise ratio R_{SN}. The randomly fluctuating Rabi frequency is

$$\Omega_{\mathrm{rand}}(t) = \Omega(t)[1 + \mathrm{rand}(t,\ \eta)], \tag{11}$$

where rand is a function generating a random number in $[-\eta,\ \eta]$. We plot three AWGN-mixed waveforms with $R_{\mathrm{SN}} = 10$ and randomly fluctuating waveforms with $\eta = 0.5$ in Figs. 6(a) and 6(c), respectively, based on which the time evolution of the ESST performance for the cyclohexylmethanol sample is plotted in Figs. 6(b) and 6(d). It is apparent that the waveforms in Figs. 6(a) and 6(c) are deformed greatly, but the time evolution of the ESST performance is influenced little by either the AWGN or the random fluctuations in the three pulses, and high-fidelity ($\mathcal{D} = 0.994$) ESST can be finally achieved. In fact, the realistic signal-to-noise ratio is usually lower than that considered in Fig. 6. Figure 6 demonstrates that the influence of random amplitude noise, including AWGN and random fluctuations, on the ESST performance is negligible. The reason lies in the fact that AWGN and random fluctuations have random absolute values and random plus and minus signs, which means that the valid pulse areas for the two interfering paths remain unchanged.

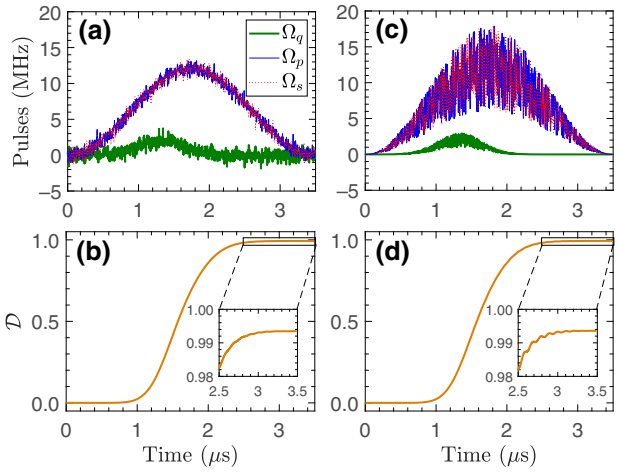

FIG. 6. (a) Waveforms of three AWGN-mixed pulses with $R_{\mathrm{SN}} = 10$. (b) Time evolution of $\mathcal{D}$ using the pulse waveforms in (a). (c) Waveforms of three randomly fluctuating pulses with $\eta = 0.5$. (d) Time evolution of $\mathcal{D}$ using the pulse waveforms in (c). $dt = 10$ ns, and other parameters are the same as in Fig. 5.

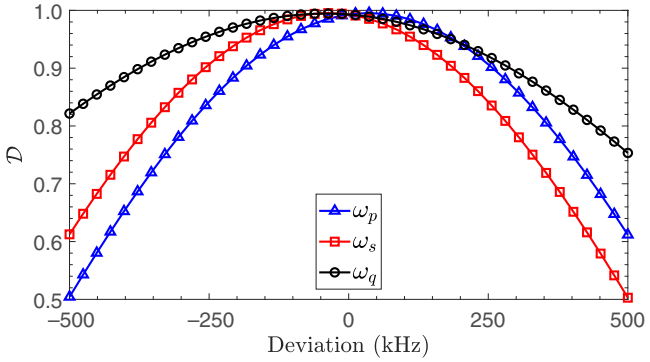

FIG. 7. Effect of deviations of each pulse frequency on the ESST performance for the cyclohexylmethanol sample. The parameters are the same as in Fig. 6.

Because of imprecise apparatus or imperfect control of the generation of the three pulses at fixed frequencies, the pulse frequencies may drift to some extent. The effect of deviations of each pulse frequency on the ESST performance for the cyclohexylmethanol sample is plotted in Fig. 7, from which we learn that the ESST performance is sensitive to the frequency deviation of each pulse (i.e., the detuning of the corresponding transition), since the two-path-interference approach is founded on the resonant regime for both the one-photon and the two-photon coupling path. A larger ratio of detuning to Rabi frequency will usually spoil the intended dynamics more significantly. In Fig. 7, however, the line for the frequency deviation of pulse q, which has the smallest Rabi frequency, has the highest $\mathcal{D}$, which is because the effective Rabi frequency ($\max\{\Omega_{\mathrm{eff}}\} = 1.2$ MHz) of the two-photon coupling path is less than Ω_q. To summarize, the present approach requires relatively precise control of the pulse frequencies. As a matter of fact, this is a common issue in the existing schemes [33,34,38,46–48,50–52], especially for schemes in the resonant regime [38,46–48,50,51]. To this end, state-of-the-art quantum optimal control techniques may give some alternative insights [54,55].

C. Energy relaxation

The states of the cyclohexylmethanol molecules used in the cyclic three-state configuration are three relatively low rotational levels and have long coherence times. However, there is a small probability that higher states may relax into lower states. Here we assume the lifetimes of $|2\rangle$ and $|3\rangle$ to

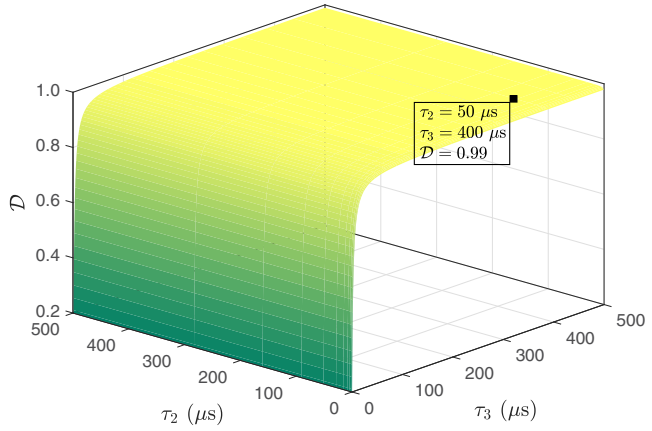

FIG. 8. Final ESST performance for the cyclohexylmethanol sample with varying τ_2 and τ_3. The parameters are the same as in Fig. 6.

be τ_2 and τ_3, respectively, and then $\gamma_{1,2} = |\mu_b|/[\tau_2(|\mu_a| + |\mu_b| + |\mu_c|)]$, $\gamma_{3,2} = |\mu_c|/[\tau_2(|\mu_a| + |\mu_b| + |\mu_c|)]$, $\gamma_{4,2} = |\mu_a|/[\tau_2(|\mu_a| + |\mu_b| + |\mu_c|)]$, and $\gamma_{1,3} = 1/\tau_3$. For simplicity, the rotational state $|4\rangle$ is assumed to be steady, since $|4\rangle$ is a lower state than $|2\rangle$ and $|3\rangle$, and, besides, $|4\rangle$ is populated very little.

Figure 8 shows the effect of varying τ_2 and τ_3 on the ESST performance for the cyclohexylmethanol sample. It is apparent that even a near-zero τ_2 hardly affects the performance of the ESST, since $|2\rangle$ is not populated during the whole enantiomer-selective process. To achieve high-fidelity ($\mathcal{D} > 0.99$) ESST of the cyclohexylmethanol sample, $\tau_2 > 50\ \mu s$ and $\tau_3 > 400\ \mu s$ are suficient. The lifetimes of rotational states are seldom considered to be one of the main factors that affect the performance of enantiomer-selective tasks on chiral molecules in schemes based on microwave spectroscopy. On the one hand, the electric dipole couplings allow fast implementation of enantiomer-selective tasks. On the other hand, the rotational states that are used to form a cyclic three-state configuration have long radiative lifetimes, which are usually over 1 μs.

V. FURTHER APPLICATIONS OF FINISHED ESST

The ESST scheme using two-path interference, once it is finished, provides discrimination of chiral molecules, which can be then followed by other enantiomer-selective tasks on chiral molecules. Without being limited by the enantiomeric excess of the sample, molecules of a certain handedness (either left- or right-handedness is possible; see Appendix C) can be selectively excited into the higher state $|3\rangle$, while molecules of the other handedness remain in the lower state $|1\rangle$. Owing to the energy difference between the two enantiomers, the molecules excited into the higher state $|3\rangle$ can be selectively ionized by applying a resonantly enhanced multiphoton ionization scheme, and then enantioseparation can be implemented by using an electric field to remove the ionized molecules [50,60].

In addition, the finished ESST can be applied to determine the enantiomeric excess by combining it with the technique of M3WM. Taking cyclohexylmethanol molecules as an example, an extra three-state cyclic configuration $|2_{02}\rangle \leftrightarrow |3_{03}\rangle \leftrightarrow |3_{13}\rangle \leftrightarrow |2_{02}\rangle$ is introduced for the purpose of M3WM, as shown in Fig. 9(a). First of all, the ESST is executed with three synchronous pulses in the two-path interference scheme, as shown in Fig. 9(b). Then two new microwave fields are imposed for M3WM. The earlier field, at a frequency of 7035.9 MHz, serves as the "drive" pulse, with a pulse area $\pi/2$, which excites the molecules in $|2_{02}\rangle$ to make them evolve with the maximum coherence between $|2_{02}\rangle$ and $|3_{03}\rangle$. A following "twist" pulse at 2017.5 MHz, with a pulse area π, shifts the population from $|3_{03}\rangle$ into $|3_{13}\rangle$ so as to create a coherence between the states $|2_{02}\rangle$ and $|3_{13}\rangle$.

Afterwards, in the form of the free-induction decay of the sample, a molecular signal that is mutually orthogonal to the drive and twist fields is created and can be recorded using Fourier-transform microwave spectroscopy

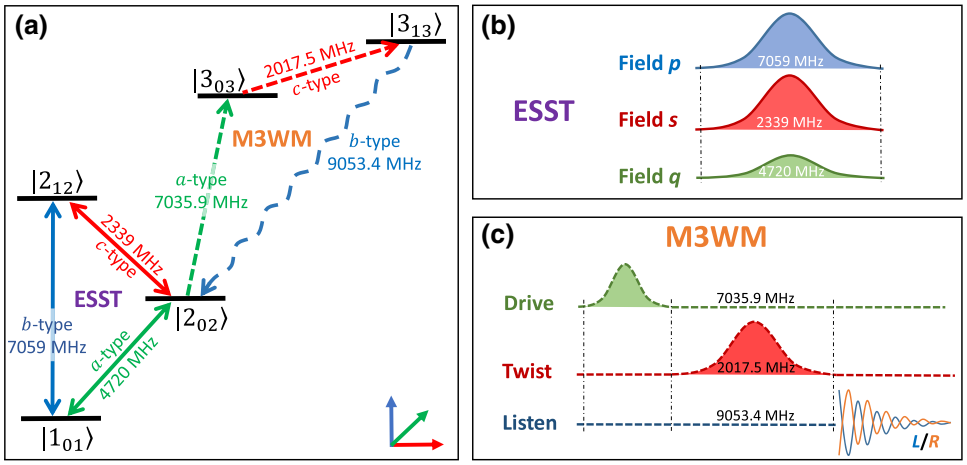

FIG. 9. (a) Two three-state cyclic configurations combining ESST and M3WM. (b) Diagram of the pulse scheme for ESST. (c) Diagram of the pulse scheme for M3WM.

techniques [61]. A diagram of the pulse scheme for M3WM is shown in Fig. 9(c). The intensity of this induced signal, i.e., the "listen" field, is proportional to [62]

$$e_e|\mu_a\cdot(\mu_b\times\mu_c)|\cos\left[2\pi\omega t+\frac{\pi\mu_a\cdot(\mu_b\times\mu_c)}{2|\mu_a\cdot(\mu_b\times\mu_c)|}\right], \tag{12}$$

where e_e denotes the enantiomeric excess, and ω the frequency of the listen transition, i.e., 9053.4 MHz. Because the sign of $\mu_a\cdot(\mu_b\times\mu_c)/|\mu_a\cdot(\mu_b\times\mu_c)|$ is enantiomer-dependent, the sign of the listen signal is dependent on the choice of the enantiomer excited in the ESST process. Finally, by taking a sample with a known enantiomeric excess as a reference and normalizing the signal intensity of this sample, the enantiomeric excess of a target sample can be determined according to the sign of the listen field and a comparison of the intensity of the signals between the target and reference samples. Note that the M3WM is based on a finished ESST, and so it works only for the molecules of one enantiomer that have been selectively excited in the ESST process. Therefore, even when the molecular sample is a racemic mixture of enantiomers, a listen signal of definite intensity can be detected, which is different from the conventional M3WM technique, where a nonzero net signal arises only if one of the enantiomers is in excess [41–43].

In addition, as an alternative to the commonly used means in which the drive pulse is followed by the twist pulse, here we propose two other ways to obtain maximum coherence in the M3WM between $|2_{02}\rangle$ and $|3_{13}\rangle$. The two ways are both based on the two-photon processes $|2_{02}\rangle\leftrightarrow|3_{03}\rangle\leftrightarrow|3_{13}\rangle$ with two synchronous pulses, one for the transition $|2_{02}\rangle\leftrightarrow|3_{03}\rangle$, with Rabi frequency Ω_d, and the other for $|3_{03}\rangle\leftrightarrow|3_{13}\rangle$, with Rabi frequency Ω_t. One way to obtain maximum coherence between $|2_{02}\rangle$ and $|3_{13}\rangle$ is to form an effective $|2_{02}\rangle\leftrightarrow|3_{13}\rangle$ coupling through the adiabatic elimination of $|3_{03}\rangle$ with a large one-photon detuning Δ', which is similar to what is done with the two-photon path in the two-path interference in ESST. Then, by controlling the pulse area so that $\int\Omega_d\Omega_t/2\Delta'\,dt=\pi/2$, the maximum coherence between $|2_{02}\rangle$ and $|3_{13}\rangle$ can be attained. The other way is based on a resonant stimulated Raman process, and the conditions are the relation $\Omega_d=(\sqrt{2}+1)\Omega_t$ and that the pulse area satisfies $\int\sqrt{\Omega_d^2+\Omega_t^2}\,dt=\pi$, which consumes a shorter time than the method using the second-order effective $|2_{02}\rangle\leftrightarrow|3_{13}\rangle$ coupling. Differently from the commonly used means, the latter two ways implement the maximum coherence between $|2_{02}\rangle$ and $|3_{13}\rangle$ in just one step, and the intermediate coherence between $|2_{02}\rangle$ and $|3_{03}\rangle$ is unnecessary.

VI. CONCLUSION

We present a two-path interference scheme for ESST of chiral molecules. Two interfering paths are constructed by use of one- and two-photon $|1\rangle\leftrightarrow|3\rangle$ transitions. The phase difference of π in the one-photon path between the two enantiomers enables the interference to be made destructive for one enantiomer but constructive for the other, which therefore results in entirely different population distributions of the two enantiomers. The simulated application of the present scheme to a cyclohexylmethanol sample demonstrates that high-fidelity ESST can be achieved, even when unwanted transitions, imperfect initial states, finite time resolution in the pulse shaping, control errors, and finite lifetimes of higher energy levels are taken into account. Furthermore, we can seek applications of the ESST, after it is finished, in enantioseparation and in determining enantiomeric excesses.

The two-path interference scheme is distinct from the existing schemes for enantiomer-selective state transfer of chiral molecules. On the one hand, the two-path interference scheme is faster than adiabatic schemes that need slowly varying drive fields. On the other hand, the scheme can be performed with two separate, partially overlapping, or synchronous paths, which allows more flexibility in the pulse sequences than do cyclic-population-transfer schemes depending on a fixed pulse order. In addition, compared with the recently developed shortcut-to-adiabatic schemes with synchronous pulses, the two-path interference scheme is not limited by the pulse waveforms and the matching relations among the pulse amplitudes. Finally, two alternative techniques for the implementation of maximum coherence in M3WM are presented that are different from the commonly used means.

ACKNOWLEDGMENTS

This work was supported by the National Natural Science Foundation of China (NSFC) (Grants No. 11675046, No. 21973023, and No. 11804308), the Program for Innovation Research of Science in Harbin Institute of Technology (Grant No. A201412), the Postdoctoral Scientific Research Developmental Fund of Heilongjiang Province (Grant No. LBH-Q15060), and the National Basic Research Program of China (Grant No. 2014CB340203).

APPENDIX A: EFFECTIVE HAMILTONIAN FOR TWO ENANTIOMERS

By solving the Schrödinger equation $i\,\partial|\psi(t)\rangle/\partial t=\hat{H}_{L,R}|\psi(t)\rangle$, where $|\psi(t)\rangle=c_1|1\rangle+c_2|2\rangle+c_3|3\rangle$ is the evolving state, with the normalization relation $|c_1|^2+$

$|c_2|^2 + |c_3|^2 = 1$, one can obtain

$$\begin{aligned} i\dot{c}_1 &= \frac{\Omega_p}{2}\mathcal{C}_2 \pm \frac{\Omega_q}{2}c_3, \\ i\dot{\mathcal{C}}_2 &= \Delta\mathcal{C}_2 + \frac{\Omega_p}{2}c_1 + \frac{\Omega_s}{2}c_3, \\ i\dot{c}_3 &= \frac{\Omega_s}{2}\mathcal{C}_2 \pm \frac{\Omega_q}{2}c_1, \end{aligned} \tag{A1}$$

with $\mathcal{C}_2 = e^{-i\Delta t}c_2$. A large Δ makes $|i\dot{\mathcal{C}}_2| \ll |\Delta\mathcal{C}_2|$, and thus we can set $\dot{\mathcal{C}}_2 = 0$, which gives

$$\mathcal{C}_2 = -\frac{1}{\Delta}\left(\frac{\Omega_p}{2}c_1 + \frac{\Omega_s}{2}c_3\right). \tag{A2}$$

By substituting Eq. (A2) into Eq. (A1), one can get

$$\begin{aligned} i\dot{c}_1 &= -\frac{\Omega_p^2}{4\Delta}c_1 - \left(\frac{\Omega_p\Omega_s}{4\Delta} \mp \frac{\Omega_q}{2}\right)c_3, \\ i\dot{c}_3 &= -\frac{\Omega_s^2}{4\Delta}c_3 - \left(\frac{\Omega_p\Omega_s}{4\Delta} \mp \frac{\Omega_q}{2}\right)c_1. \end{aligned} \tag{A3}$$

Conversely, according to Eq. (A3), an effective Hamiltonian for $\hat{H}_{L,R}$ in Eq. (2) can be developed:

$$\begin{aligned} \hat{H}^e_{L,R} = &\frac{\Omega_p^2}{4\Delta}|1\rangle\langle 1| + \frac{\Omega_s^2}{4\Delta}|3\rangle\langle 3| \\ &+ \left(\frac{\Omega_p\Omega_s}{4\Delta} \mp \frac{\Omega_q}{2}\right)(|1\rangle\langle 3| + |3\rangle\langle 1|), \end{aligned} \tag{A4}$$

in which we have neglected the global phase. The first two terms in Eq. (A4) are the Stark shifts of $|1\rangle$ and $|3\rangle$, while the last term denotes the effective interaction between $|1\rangle$ and $|3\rangle$, with an effective Rabi frequency $\Omega_{\text{eff}} \equiv \Omega_p\Omega_s/2\Delta$. Further, the Stark-shift terms can be dropped when $\Omega_p = \Omega_s$ because of the completeness relation $|1\rangle\langle 1| + |3\rangle\langle 3| = \hat{\mathcal{I}}$, $\hat{\mathcal{I}}$ being the unit operator.

APPENDIX B: MASTER EQUATION WITH UNWANTED TRANSITIONS AND AN IMPERFECT INITIAL STATE

The five transitions considered, $|1\rangle \leftrightarrow |2\rangle$, $|1\rangle \leftrightarrow |3\rangle$, $|2\rangle \leftrightarrow |3\rangle$, $|1\rangle \leftrightarrow |4\rangle$, and $|2\rangle \leftrightarrow |4\rangle$, have transition frequencies $\omega_{12} = 7059$ MHz (b-type), $\omega_{13} = 4720$ MHz (a-type), $\omega_{23} = 2339$ MHz (c-type), $\omega_{14} = 2575$ MHz (c-type), and $\omega_{24} = 4484$ MHz (a-type), respectively. The a-type, b-type, and c-type transitions are driven by orthogonal pulses q at a frequency $\omega_q = \omega_{13}$, p at a frequency $\omega_p = \omega_{12} - \Delta$, and s at a frequency $\omega_s = \omega_{23} - \Delta$, respectively. By choosing appropriate axes such that each transition dipole moment and its driving field have the same orientation, the evolution of the two enantiomers can be governed by the Hamiltonian

$$\begin{aligned} \hat{H}_{L,R} = &\sum_{j=2}^{4}\omega_{1j}|j\rangle\langle j| + [\Omega_p\cos\omega_p t|1\rangle\langle 2| \\ &\pm \Omega_q\cos\omega_q t(|1\rangle\langle 3| + |2\rangle\langle 4|) \\ &+ \Omega_s\cos\omega_s t(|2\rangle\langle 3| + |1\rangle\langle 4|) + \text{H.c.}]. \end{aligned} \tag{B1}$$

An experiment based on the present proposal is assumed to be carried out with an ultracold cyclohexylmethanol sample, the temperature of which should be low enough that all molecules can be prepared perfectly in the initial state $|1\rangle$. Buffer-gas cooling and supersonic expansion are two possible tools for cooling the molecular samples. In recent experiments, molecular samples were cooled to a temperature of around 5–10 K by using a cryogenic buffer-gas cell [41,42,46]. Supersonic expansion can cool molecules to rotational temperatures of about 1–2 K [43,45,47,48]. Here we assume that the present proposal is carried out at a relatively low temperature, and all molecules are prepared initially in a weakly mixed state with a density operator $\hat{\rho}_0 = 0.998|1\rangle\langle 1| + 0.001|2\rangle\langle 2| + 0.001|3\rangle\langle 3|$, which means that the initial state contains a small amount of $|2\rangle$ and $|3\rangle$ with the same mixed probability 0.001. Then the time evolution of the density operator $\hat{\rho}$ can be governed by a Markovian master equation when the energy relaxations of higher-energy states are taken into account:

$$\begin{aligned} \frac{\partial\hat{\rho}}{\partial t} = &i\hat{\rho}\hat{H}_{L,R} - i\hat{H}_{L,R}\hat{\rho} \\ &- \sum_{j=2}^{4}\frac{\gamma_{1,j}}{2}\left(\hat{\sigma}^\dagger_{1,j}\hat{\sigma}_{1,j}\hat{\rho} - 2\hat{\sigma}_{1,j}\hat{\rho}\hat{\sigma}^\dagger_{1,j} + \hat{\rho}\hat{\sigma}^\dagger_{1,j}\hat{\sigma}_{1,j}\right) \\ &- \sum_{k=3,4}\frac{\gamma_{k,2}}{2}\left(\hat{\sigma}^\dagger_{k,2}\hat{\sigma}_{k,2}\hat{\rho} - 2\hat{\sigma}_{k,2}\hat{\rho}\hat{\sigma}^\dagger_{k,2} + \hat{\rho}\hat{\sigma}^\dagger_{k,2}\hat{\sigma}_{k,2}\right), \end{aligned} \tag{B2}$$

where $\gamma_{m,n}$ is the relaxation rate from $|n\rangle$ to $|m\rangle$, and $\hat{\sigma}_{m,n} \equiv |m\rangle\langle n|$ is the relaxation operator.

APPENDIX C: DEPENDENCE OF THE ENANTIOMER-SELECTIVE EXCITATION ON FIELD PHASES

Dependence of enantiomer-selective tasks on the phases of fields is a common property of the existing schemes, and it can also be used to switch the excitation of the two enantiomers. The phases of the three microwave fields are chosen as zero for convenience, but this is of course not the only possible choice. When nonzero phases of the three microwave fields are taken into account, the effective

Hamiltonian Eq. (3) for the two enantiomers becomes

$$\hat{H}_{L,R}^{\text{eff}} = \frac{\Omega_q e^{i\phi_q t} \mp \Omega_{\text{eff}} e^{i(\phi_p - \phi_s)t}}{2} |1\rangle\langle 3| + \text{H.c.} \qquad \text{(C1)}$$

From Eq. (C1), we find that the three field phases have a decisive effect on the properties of the two-path interference for the two enantiomers. For the interference between the one- and two-photon $|1\rangle \leftrightarrow |3\rangle$ transitions to be constructive for one enantiomer but destructive for the other, the condition is

$$\phi_q - \phi_p + \phi_s = n\pi, \quad n \in \text{integers}, \qquad \text{(C2)}$$

where, when n is odd (even), the two-path interference is constructive for left-handed (right-handed) molecules but destructive for right-handed (left-handed) ones. Therefore, a change of phase by π in any one of the three fields will invert the interference properties of the two enantiomers and switch the excitation of the two enantiomers.

[1] K. T. Barrett, A. J. Metrano, P. R. Rablen, and S. J. Miller, Spontaneous transfer of chirality in an atropisomerically enriched two-axis system, Nature **509**, 71 (2014).

[2] M. Kaushik, K. Basu, C. Benoit, C. M. Cirtiu, H. Vali, and A. Moores, Cellulose nanocrystals as chiral inducers: Enantioselective catalysis and transmission electron microscopy 3D characterization, J. Am. Chem. Soc. **137**, 6124 (2015).

[3] X. Jiang, J. J. Beiger, and J. F. Hartwig, Stereodivergent allylic substitutions with aryl acetic acid esters by synergistic iridium and lewis base catalysis, J. Am. Chem. Soc. **139**, 87 (2017).

[4] J. Gal, The discovery of stereoselectivity at biological receptors: Arnaldo piutti and the taste of the asparagine enantiomers-history and analysis on the 125th anniversary, Chirality **24**, 959 (2012).

[5] A. M. Intlekofer, R. G. Dematteo, S. Venneti, L. W. S. Finley, C. Lu, A. R. Judkins, A. S. Rustenburg, P. B. Grinaway, J. D. Chodera, J. R. Cross, and C. B. Thompson, Hypoxia induces production of l-2-hydroxyglutarate, Cell Metab. **22**, 304 (2015).

[6] Y. Chen and W. Ma, The origin of biological homochirality along with the origin of life, PLOS Comput. Biol. **16**, e1007592 (2020).

[7] R. Ma, B. Wang, S. Lu, Y. Zhang, L. Yin, J. Huang, S. Deng, Y. Wang, and G. Yu, Characterization of pharmaceutically active compounds in Dongting lake, China: Occurrence, chiral profiling and environmental risk, Sci. Total Environ. **557–558**, 268 (2016).

[8] C. L. Amorim, I. S. Moreira, A. R. Ribeiro, L. H. Santos, C. DelerueMatos, M. E. Tiritan, and P. M. Castro, Treatment of a simulated wastewater amended with a chiral pharmaceuticals mixture by an aerobic granular sludge sequencing batch reactor, Int. Biodeter. Biodegr. **115**, 277 (2016).

[9] E. Sanganyado, Z. Lu, Q. Fu, D. Schlenk, and J. Gan, Chiral pharmaceuticals: A review on their environmental occurrence and fate processes, Water Res. **124**, 527 (2017).

[10] A. R. Ribeiro, P. M. L. Castro, and M. E. Tiritan, Chiral pharmaceuticals in the environment, Environ. Chem. Lett. **10**, 239 (2012).

[11] K. Bodenhöfer, A. Hierlemann, J. Seemann, G. Gauglitz, B. Koppenhoefer, and W. Gpel, Chiral discrimination using piezoelectric and optical gas sensors, Nature **387**, 577 (1997).

[12] R. McKendry, M.-E. Theoclitou, T. Rayment, and C. Abell, Chiral discrimination by chemical force microscopy, Nature **391**, 566 (1998).

[13] G. Rikken and E. Raupach, Enantioselective magnetochiral photochemistry, Nature **405**, 932 (2000).

[14] H. Zepik, E. Shavit, M. Tang, T. R. Jensen, K. Kjaer, G. Bolbach, L. Leiserowitz, I. Weissbuch, and M. Lahav, Chiral amplification of oligopeptides in two-dimensional crystalline self-assemblies on water, Science **295**, 1266 (2002).

[15] R. Bielski and M. Tencer, Absolute enantioselective separation: Optical activity ex machina, J. Sep. Sci. **28**, 2325 (2005).

[16] R. Bielski and M. Tencer, A possible path to the RNA world: Enantioselective and diastereoselective purification of ribose, Orig. Life Evol. Biosphere **37**, 167 (2007).

[17] R. P. Cameron, S. M. Barnett, and A. M. Yao, Discriminatory optical force for chiral molecules, New J. Phys. **16**, 013020 (2014).

[18] D. S. Bradshaw, K. A. Forbes, J. M. Leeder, and D. L. Andrews, Chirality in optical trapping and optical binding, Photonics **2**, 483 (2015).

[19] D. S. Bradshaw and D. L. Andrews, Laser optical separation of chiral molecules, Opt. Lett. **40**, 677 (2015).

[20] R. P. Cameron, J. B. Götte, and S. M. Barnett, Chiral rotational spectroscopy, Phys. Rev. A **94**, 032505 (2016).

[21] A. A. Milner, J. A. M. Fordyce, I. MacPhail-Bartley, W. Wasserman, V. Milner, I. Tutunnikov, and I. S. Averbukh, Controlled Enantioselective Orientation of Chiral Molecules with an Optical Centrifuge, Phys. Rev. Lett. **122**, 223201 (2019).

[22] A. Yachmenev, J. Onvlee, E. Zak, A. Owens, and J. Küpper, Fieldinduced Diastereomers for Chiral Separation, Phys. Rev. Lett. **123**, 243202 (2019).

[23] N. Berova, L. D. Bari, and G. Pescitelli, Application of electronic circular dichroism in configurational and conformational analysis of organic compounds, Chem. Soc. Rev. **36**, 914 (2007).

[24] L. A. Nafie, *Vibrational Optical Activity* (Wiley, New York, 2011).

[25] L. D. Barron, F. Zhu, L. Hecht, G. E. Tranter, and N. W. Isaacs, Raman optical activity: An incisive probe of molecular chirality and biomolecular structure, J. Mol. Struct. **834–836**, 7 (2007).

[26] L. D. Barron, *Molecular Light Scattering and Optical Activity* (Cambridge University Press, Cambridge, 2004).

[27] L. A. Nafie, Handedness detected by microwaves, Nature **497**, 446 (2013).

[28] D. Patterson and M. Schnell, New studies on molecular chirality in the gas phase: Enantiomer differentiation and determination of enantiomeric excess, Phys. Chem. Chem. Phys. **16**, 11114 (2014).

[29] J. R. Rouxel, M. Kowalewski, and S. Mukamel, Photoinduced molecular chirality probed by ultrafast resonant X-ray spectroscopy, Struct. Dyn. **4**, 044006 (2017).
[30] J. R. Rouxel, M. Kowalewski, and S. Mukamel, Diffraction-detected sum frequency generation: Novel ultrafast X-ray probe of molecular dynamics, J. Phys. Chem. Lett. **9**, 3392 (2018).
[31] K. Hiramatsu, H. Kano, and T. Nagata, Raman optical activity by coherent anti-Stokes Raman scattering spectral interferometry, Opt. Express **21**, 13515 (2013).
[32] T. K. Begzjav, Z. Zhang, M. O. Scully, and G. S. Agarwal, Enhanced signals from chiral molecules via molecular coherence, Opt. Express **27**, 13965 (2019).
[33] P. Král and M. Shapiro, Cyclic Population Transfer in Quantum Systems with Broken Symmetry, Phys. Rev. Lett. **87**, 183002 (2001).
[34] P. Král, I. Thanopulos, M. Shapiro, and D. Cohen, Two-Step Enantioselective Optical Switch, Phys. Rev. Lett. **90**, 033001 (2003).
[35] P. Král, I. Thanopulos, and M. Shapiro, Colloquium: Coherently controlled adiabatic passage, Rev. Mod. Phys. **79**, 53 (2007).
[36] K. Bergmann, H. Theuer, and B. W. Shore, Coherent population transfer among quantum states of atoms and molecules, Rev. Mod. Phys. **70**, 1003 (1998).
[37] N. V. Vitanov, A. A. Rangelov, B. W. Shore, and K. Bergmann, Stimulated Raman adiabatic passage in physics, chemistry, and beyond, Rev. Mod. Phys. **89**, 015006 (2017).
[38] Y. Li and C. Bruder, Dynamic method to distinguish between left- and right-handed chiral molecules, Phys. Rev. A **77**, 015403 (2008).
[39] W. Z. Jia and L. F. Wei, Distinguishing left- and right-handed molecules using two-step coherent pulses, J. Phys. B: At. Mol. Opt. Phys. **43**, 185402 (2010).
[40] C. Ye, Q. Zhang, Y.-Y. Chen, and Y. Li, Determination of enantiomeric excess with chirality-dependent ac stark effects in cyclic three-level models, Phys. Rev. A **100**, 033411 (2019).
[41] D. Patterson, M. Schnell, and J. M. Doyle, Enantiomer-specific detection of chiral molecules via microwave spectroscopy, Nature **497**, 475 (2013).
[42] D. Patterson and J. M. Doyle, Sensitive Chiral Analysis via Microwave Three-Wave Mixing, Phys. Rev. Lett. **111**, 023008 (2013).
[43] V. A. Shubert, D. Schmitz, D. Patterson, J. M. Doyle, and M. Schnell, Identifying enantiomers in mixtures of chiral molecules with broadband microwave spectroscopy, Angew. Chem. Int. Ed. **53**, 1152 (2014).
[44] S. Lobsiger, C. Pérez, L. Evangelisti, K. K. Lehmann, and B. H. Pate, Molecular structure and chirality detection by Fourier transform microwave spectroscopy, J. Phys. Chem. Lett. **6**, 196 (2015).
[45] V. A. Shubert, D. Schmitz, C. Medcraft, A. Krin, D. Patterson, J. M. Doyle, and M. Schnell, Rotational spectroscopy and three-wave mixing of 4-carvomenthenol: A technical guide to measuring chirality in the microwave regime, J. Chem. Phys. **142**, 214201 (2015).
[46] S. Eibenberger, J. Doyle, and D. Patterson, Enantiomer-Specific State Transfer of Chiral Molecules, Phys. Rev. Lett. **118**, 123002 (2017).
[47] C. Pérez, A. L. Steber, S. R. Domingos, A. Krin, D. Schmitz, and M. Schnell, Coherent enantiomer-selective population enrichment using tailored microwave fields, Angew. Chem. **129**, 12686 (2017).
[48] C. Pérez, A. L. Steber, A. Krin, and M. Schnell, State-specific enrichment of chiral conformers with microwave spectroscopy, J. Phys. Chem. Lett. **9**, 4539 (2018).
[49] C. Ye, Q. Zhang, and Y. Li, Real single-loop cyclic three-level configuration of chiral molecules, Phys. Rev. A **98**, 063401 (2018).
[50] N. V. Vitanov and M. Drewsen, Highly Efficient Detection and Separation of Chiral Molecules through Shortcuts to Adiabaticity, Phys. Rev. Lett. **122**, 173202 (2019).
[51] J.-L. Wu, Y. Wang, J. Song, Y. Xia, S.-L. Su, and Y.-Y. Jiang, Robust and highly efficient discrimination of chiral molecules through threemode parallel paths, Phys. Rev. A **100**, 043413 (2019).
[52] C. Ye, Q. Zhang, Y.-Y. Chen, and Y. Li, Effective two-level models for highly efficient inner-state enantioseparation based on cyclic three-level systems of chiral molecules, Phys. Rev. A **100**, 043403 (2019).
[53] E. Hirota, Triple resonance for a three-level system of a chiral molecule, Proc. Jpn. Acad. B **88**, 120 (2012).
[54] S. J. Glaser, U. Boscain, T. Calarco, C. P. Koch, W. Köckenberger, R. Kosloff, I. Kuprov, B. Luy, S. Schirmer, T. Schulte-Herbrüggen, D. Sugny, and F. K. Wilhelm, Training Schrödinger's cat: Quantum optimal control, Eur. Phys. J. D **69**, 279 (2015).
[55] B.-J. Liu, X.-K. Song, Z.-Y. Xue, X. Wang, and M.-H. Yung, Plug-And-Play Approach to Nonadiabatic Geometric Quantum Gates, Phys. Rev. Lett. **123**, 100501 (2019).
[56] J. L. Wu and S. L. Su, Universal speeded-up adiabatic geometric quantum computation in three-level systems via counterdiabatic driving, J. Phys. A: Math. Theor. **52**, 335301 (2019).
[57] I. Powis, Photoelectron circular dichroism in chiral molecules, Adv. Chem. Phys. **138**, 267 (2008).
[58] J. Zhang, J. H. Shim, I. Niemeyer, T. Taniguchi, T. Teraji, H. Abe, S. Onoda, T. Yamamoto, T. Ohshima, J. Isoya, and D. Suter, Experimental Implementation of Assisted Quantum Adiabatic Passage in a Single Spin, Phys. Rev. Lett. **110**, 240501 (2013).
[59] B. Zhou, A. Baksic, H. Ribeiro, C. Yale, F. Heremans, P. Jerger, A. Auer, G. Burkard, A. Clerk, and D. Awschalom, Accelerated quantum control using superadiabatic dynamics in a solid-state lambda system, Nat. Phys. **13**, 330 (2017).
[60] K. Højbjerre, D. Offenberg, C. Z. Bisgaard, H. Stapelfeldt, P. F. Staanum, A. Mortensen, and M. Drewsen, Consecutive photodissociation of a single complex molecular ion, Phys. Rev. A **77**, 030702(R) (2008).
[61] T. J. Balle and W. H. Flygare, Fabry-Perot cavity pulsed Fourier transform microwave spectrometer with a pulsed nozzle particle source, Rev. Sci. Instrum. **52**, 33 (1981).
[62] J.-U. Grabow, Fourier transform microwave spectroscopy: Handedness caught by rotational coherence, Angew. Chem. Int. Ed. **52**, 11698 (2013).